Electronic supplementary information

Scalable synthesis of Na_2MVF_7 (M = Mn, Fe, and Co) as high-performance cathode materials for sodium-ion batteries

*Jiaying Liao‡, Jingchen Han‡, Jianzhi Xu, Yichen Du, Liping Duan, Yingying Sun and Xiaosi Zhou**

Jiangsu Key Laboratory of New Power Batteries, Jiangsu Collaborative Innovation Center of Biomedical Functional Materials, School of Chemistry and Materials Science, Nanjing Normal University, Nanjing 210023, China

*Corresponding authors.

E-mail: zhouxiaosi@njnu.edu.cn

‡ J. L. and J. H. contributed equally to this work.

Experimental section

Synthesis of Na_2MVF_7 (M = Mn, Fe, and Co): Na_2MVF_7 was synthesized via a solid-state reaction method using polytetrafluoroethylene $(–CF_2–CF_2–)_n$ (PTFE, Dupont, diameter < 1 μm) as a fluorine source. Typically, NaF, $MC_2O_4·2H_2O$, NH_4VO_3, and PTFE were planetary ball-milled with a molar ratio of 2:1:1.05:2 in ethanol at a speed of 500 rpm for 12 h. NH_4VO_3 was 5% excess to balance the subsequent evaporation of VF_3. After drying, the resulting mixture was pelletized and preheated at 550 °C for 1 h under flowing Ar. Thereafter, the pellet was intermediately ground to fine powder and further annealed at 650 °C for 1 h under an Ar environment to obtain the prduct of Na_2MVF_7 (M = Mn, Fe, and Co). Note that Na_2MVF_7 was economically synthesized without using expensive transition metal fluorides MF_2 and VF_3.

Materials characterization: The crystal phases of as-obtained Na_2MVF_7 (M = Mn, Fe, and Co) were characterized with an X-ray diffractometer (XRD; Rigaku, SmartLab). Rietveld approach was employed to refine the data sets using the GSAS package incorporated with the EXPGUI interface.[1] The morphology and structure of the samples were studied by scanning electron microscopy (SEM; JSM-7600F) and transmission electron microscopy (TEM; FEI Talos F200X). The elemental mappings were analyzed by energy dispersive X-ray spectroscopy (EDX) attached to the TEM instrument. Thermogravimetric analysis (TGA) was performed at a heating rate of 10 °C min^{-1} in the temperature range of 25–800 °C under an air or Ar atmosphere (Shinadzu, DTG-60H). The element species and valence states were determined by X-ray photoelectron spectroscopy (XPS; ESCALab 250Xi).

Electrochemical measurements: Before the electrochemical evaluation, Na_2MVF_7 (M = Mn, Fe, and Co) and Ketjen black (KB) were mixed by high-energy ball milling (8000D Mixer/Mill, SPEX SamplePrep) with a mass ratio of 7:2 for 30 min to enhance the electrical conductivity and reduce the particle size. The electrodes were prepared by mixing the ball-milled products (90 wt%) and poly(vinylidene fluoride) binder (10 wt%) in N-methyl-2-pyrrolidinone to obtain slurries, which were coated on aluminium foil and then dried in a vacuum oven at 80 °C. The typical mass loading of active material was about 1.5 mg cm^{-2}. The electrochemical properties of Na_2MVF_7 were evaluated using CR2032coin-type cells, which were assembled in an argon-filled glovebox (O_2 and H_2O < 0.1

ppm). For the fabrication of sodium-ion batteries, sodium metal was used as the counter electrode, 1 M $NaClO_4$ in ethylene carbonate (EC)/propylene carbonate (PC) (1:1 by volume) with 5% fluoroethylene carbonate additive was used as the electrolyte. And a Whatman glass-fiber separator was used for each cell. Cyclic voltammetry (CV) measurements were conducted on a PARSTAT 4000 electrochemical workstation in a voltage range from 1.5 to 4.5 V at scan rates of 0.1–1.0 mV s^{-1}. Electrochemical impedance spectroscopy (EIS) was carried out in the frequency range of 10^5 Hz–0.01 Hz. The cells were galvanostatically cycled on a multi-channel battery test system (Land CT2001A) in the voltage range from 1.5 to 4.5 V.

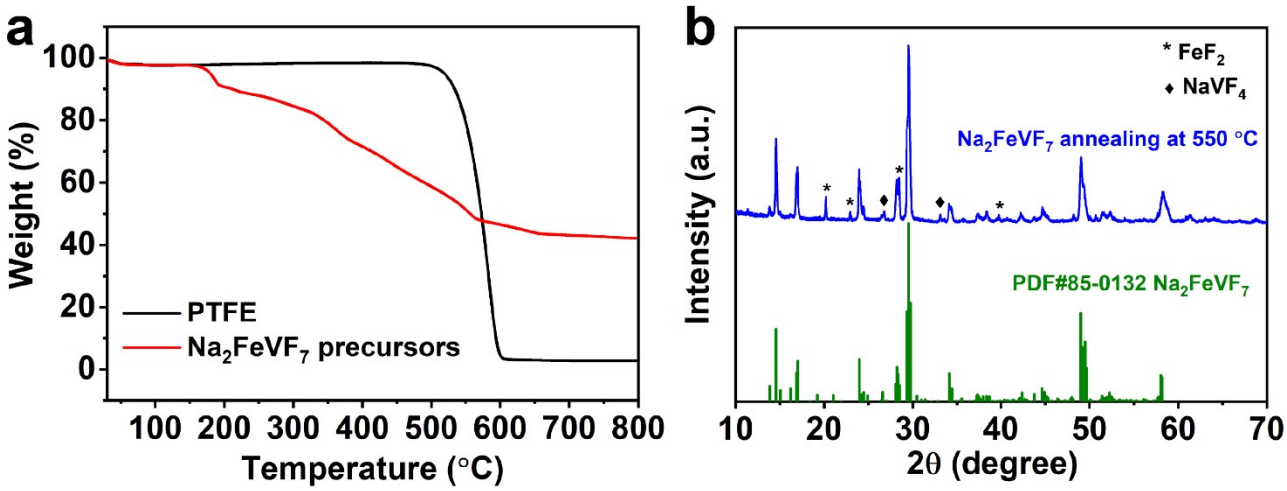

Fig. S1. (a) TGA curves of PTFE and the mixture of ball-milled Na_2FeVF_7 precursors (NaF, $FeC_2O_4 \cdot 2H_2O$, NH_4VO_3, and PTFE) under an Ar atmosphere with a temperature ramp of 10 °C min^{-1} from room temperature to 800 °C. (b) XRD pattern of the sample obtained after the first sintering.

As shown in **Fig. S1a**, the first sintering step at 550 ℃ is used to decompose of precursors and PTFE, which can produce a strong fluorinated environment. The second sintering step at 650 ℃ aims to eliminate a small amount of FeF_2 and $NaVF_4$ intermediate products after the first step of sintering to form the target product Na_2FeVF_7 (**Fig. S1b**).

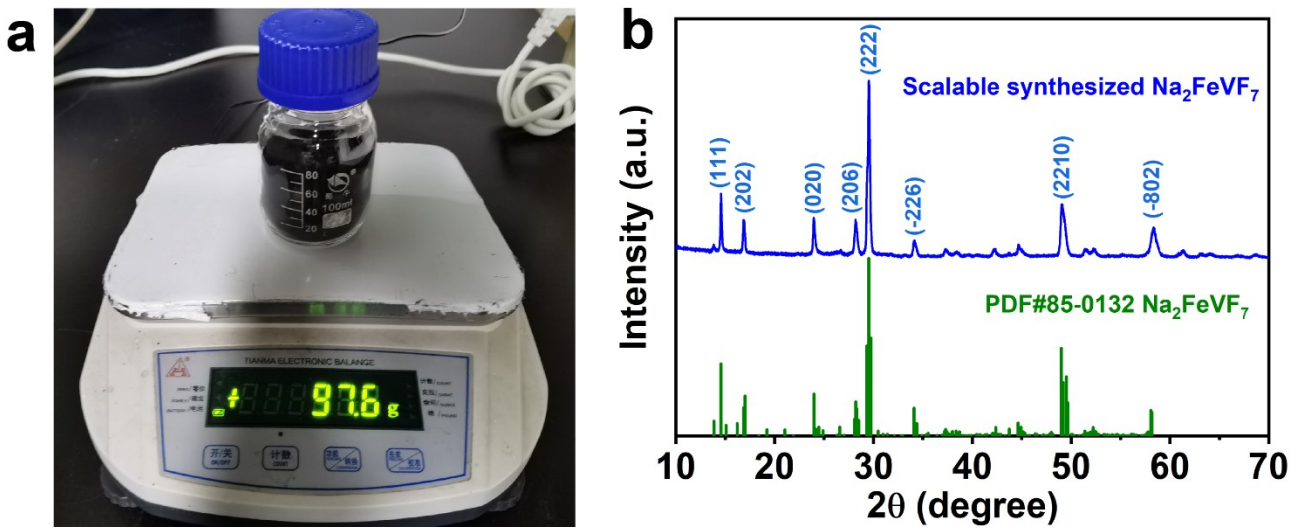

Fig. S2. (a) Digital image and (b) XRD pattern of the as-synthesized ~100 gram-scale Na_2FeVF_7 product.

Table S1. Crystallographic parameters of the Rietveld refinement for Na_2MnVF_7, Na_2FeVF_7, and Na_2CoVF_7.

Samples	**Space groups**	***a*/Å**	***b*/Å**	***c*/Å**	***β*/°**
Na_2MnVF_7	$P3_221$	7.4783(7)	7.4783(7)	18.2296(2)	90
Na_2FeVF_7	$C2/c$	12.7656(9)	7.4259(5)	24.6907(1)	100.17(8)
Na_2CoVF_7	$C2/c$	12.7066(5)	7.3706(7)	24.5919(5)	99.98(4)

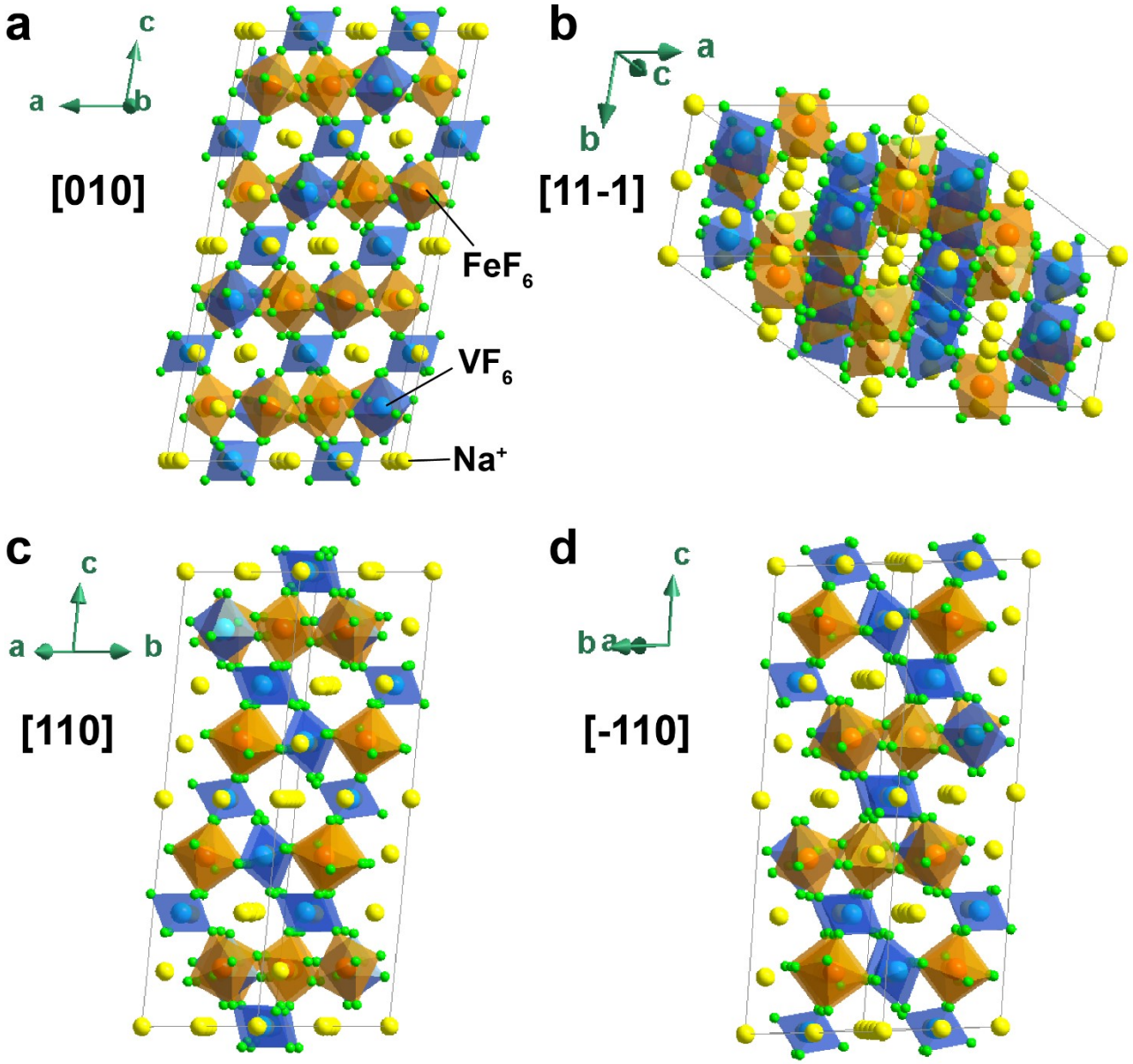

Fig. S3. Crystal structures of Na_2FeVF_7 viewing from (a) [010], (b) [11-1], (c) [110], and (d) [1-10] directions.

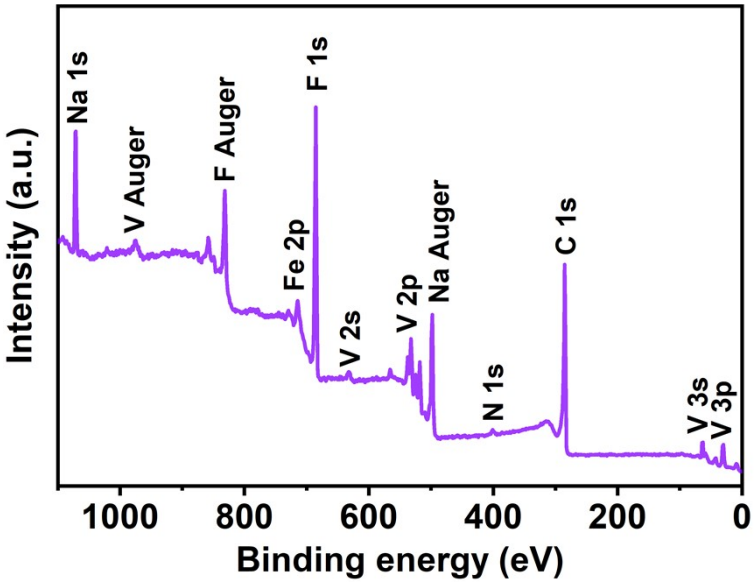

Fig. S4. XPS survey scan of Na_2FeVF_7.

As displayed in **Fig. S4**, the slight N 1s peak may be derived from the nitrogen-doped carbon obtained from the decomposition of the raw material NH_4VO_3.

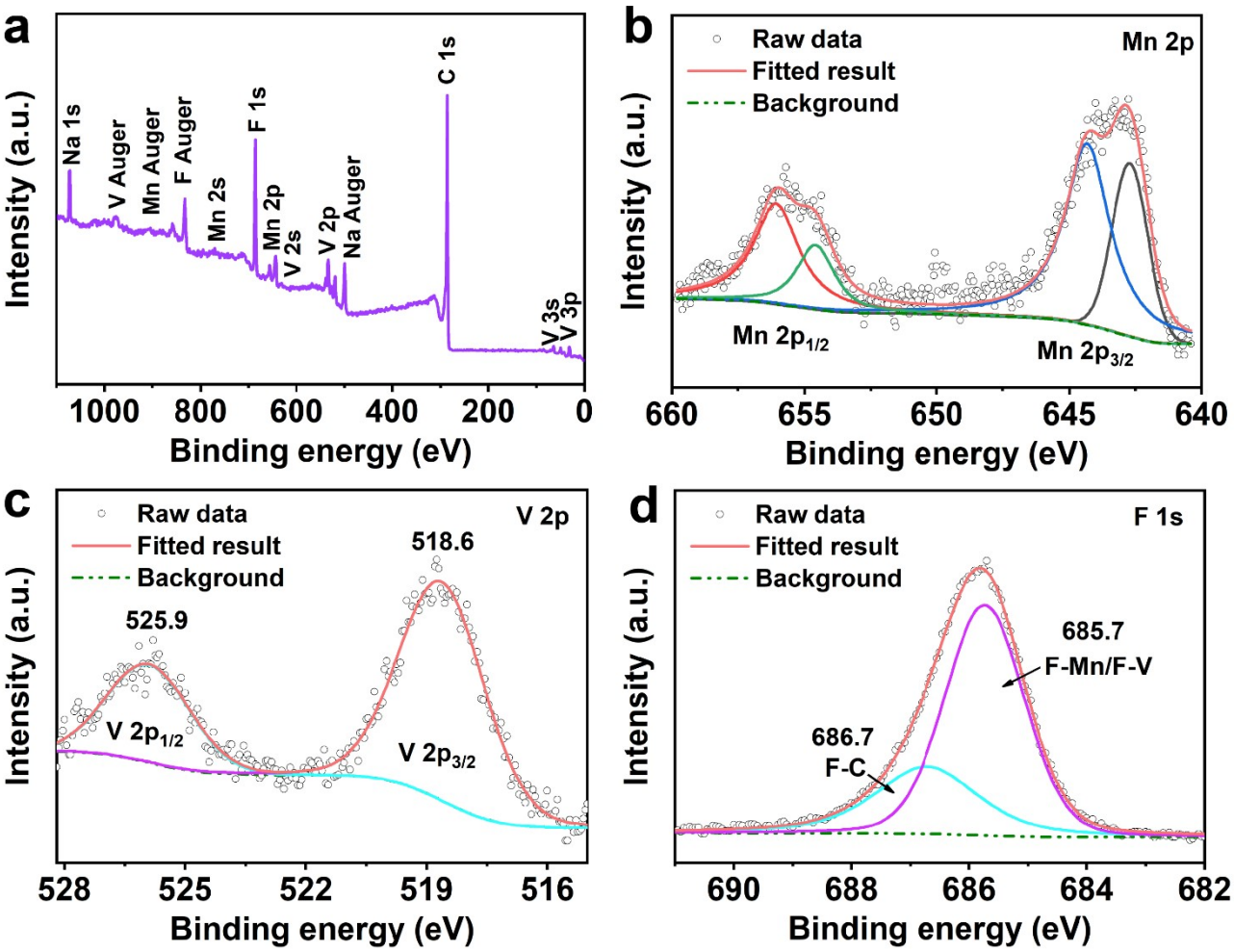

Fig. S5. XPS spectrum of Na_2MnVF_7: (a) Survey scan and high-resolution XPS spectra of (b) Mn 2p, (c) V 2p, and (d) F 1s.

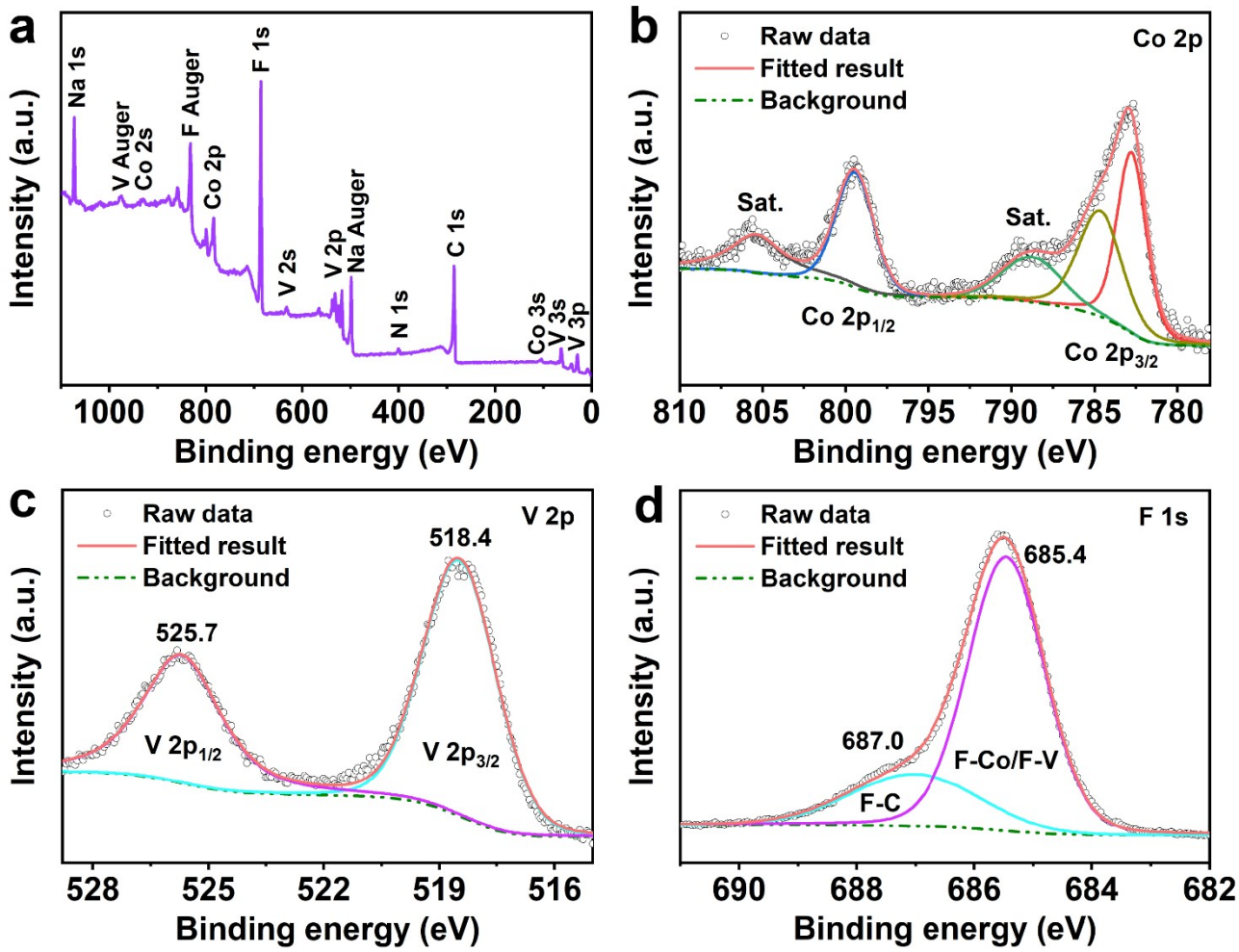

Fig. S6. XPS spectrum of Na_2CoVF_7: (a) Survey scan and high-resolution XPS spectra of (b) Co 2p, (c) V 2p, and (d) F 1s.

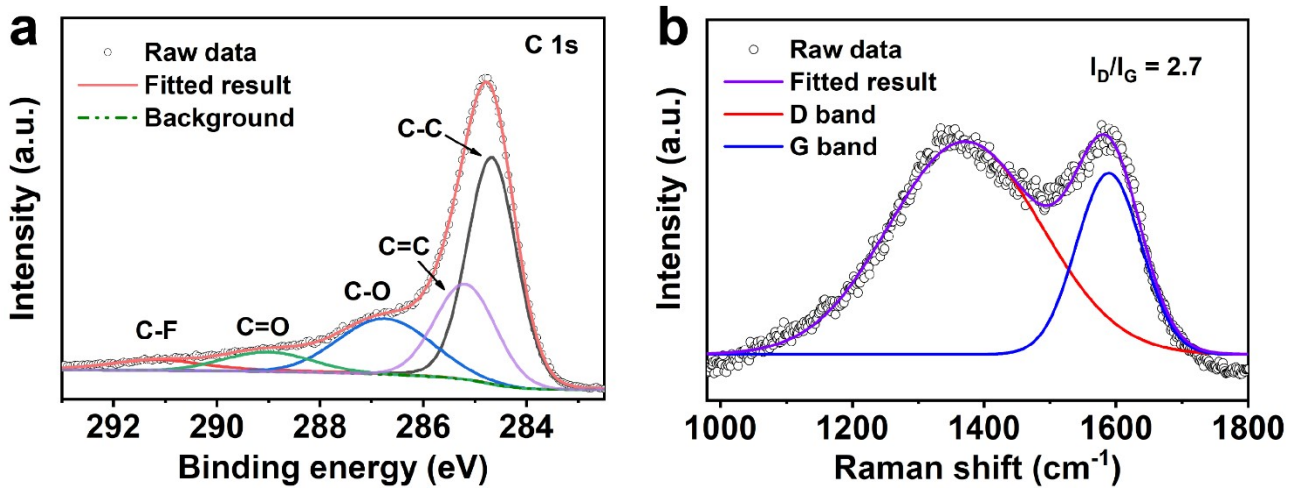

Fig. S7. (a) High-resolution C 1s XPS spectrum and (b) Raman spectrum of Na_2FeVF_7.

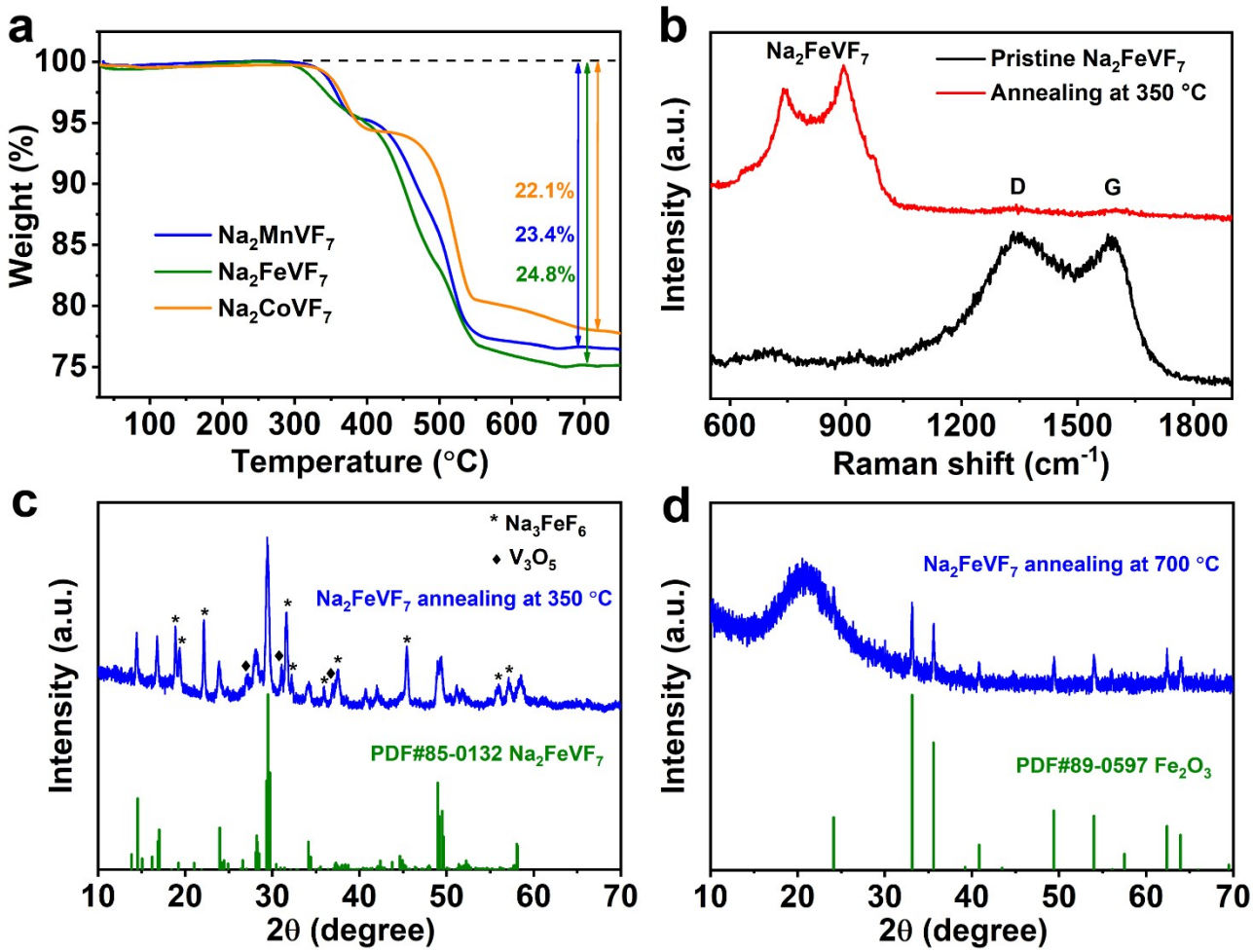

Fig. S8. (a) TGA curves of Na_2MnVF_7, Na_2FeVF_7, and Na_2CoVF_7 under an air environment at a heating rate of 10 °C min^{-1} from room temperature to 750 °C. (b) Raman spectra of Na_2FeVF_7 before and after annealing at 350 °C in air. (c, d) XRD patterns of Na_2FeVF_7 after annealing at 350 °C (c) and 700 °C (d) in air.

We choose Na_2FeVF_7 sample as a representative to analyze the decomposition process (**Fig. S8a**). As shown in **Fig. S8b**, the characteristic D and G bands of carbon almost disappear after annealing at 350 °C in air. It means that the first weight loss plateau at about 350 °C is related to the oxidation of carbon and the partial decompostion of Na_2FeVF_7 to form Na_3FeF_6 and V_3O_5 (**Fig. S8c**). After annealing at 700 °C, Na_2FeVF_7 decomposes into Fe_2O_3 and amorphous $2Na_2O{-}V_2O_5$ (**Fig. S8d**). Therefore, the second weight loss plateau is the complete oxidation of fluorides. The F element is replaced by O_2 or H_2O in the air to generate F_2/HF gas. In materials containing F, F is easily replaced by O at high temperatures (*Adv. Energy Mater.*, 2018, **8**, 1801591). The weight loss of Na_2FeVF_7 into

its oxidative products ($2Na_2O-V_2O_5$ and Fe_2O_3) is about 19.5%. Based on the wight losses displayed in **Fig. S8a**, the carbon content in Na_2MnVF_7, Na_2FeVF_7, and Na_2CoVF_7 is calculated to be approximately 4.8%, 6.6%, and 3.2%, respectively.

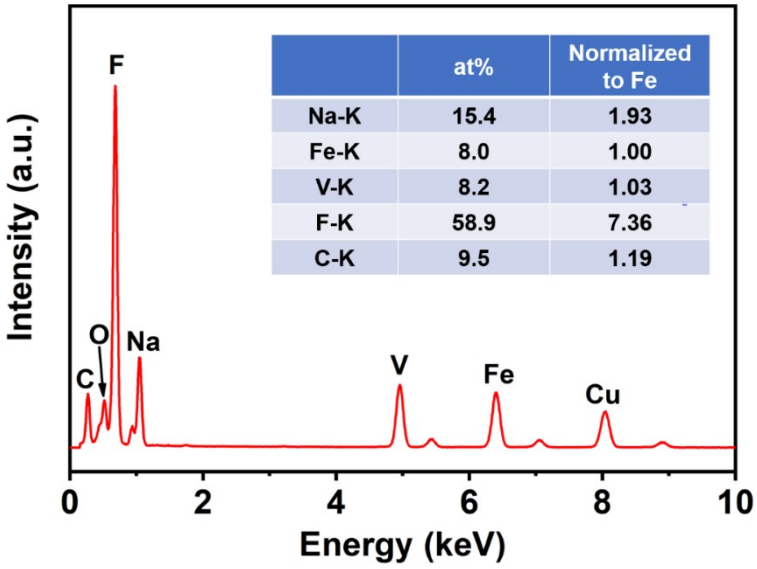

	at%	Normalized to Fe
Na-K	15.4	1.93
Fe-K	8.0	1.00
V-K	8.2	1.03
F-K	58.9	7.36
C-K	9.5	1.19

Fig. S9. EDX spectrum of Na_2FeVF_7.

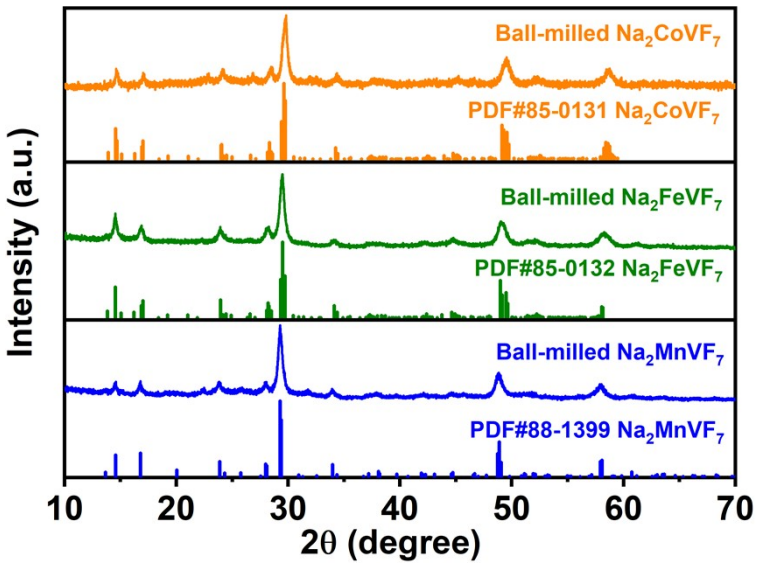

Fig. S10. XRD patterns of Na_2MnVF_7, Na_2FeVF_7, and Na_2CoVF_7 after high-energy ball milling with Ketjen black.

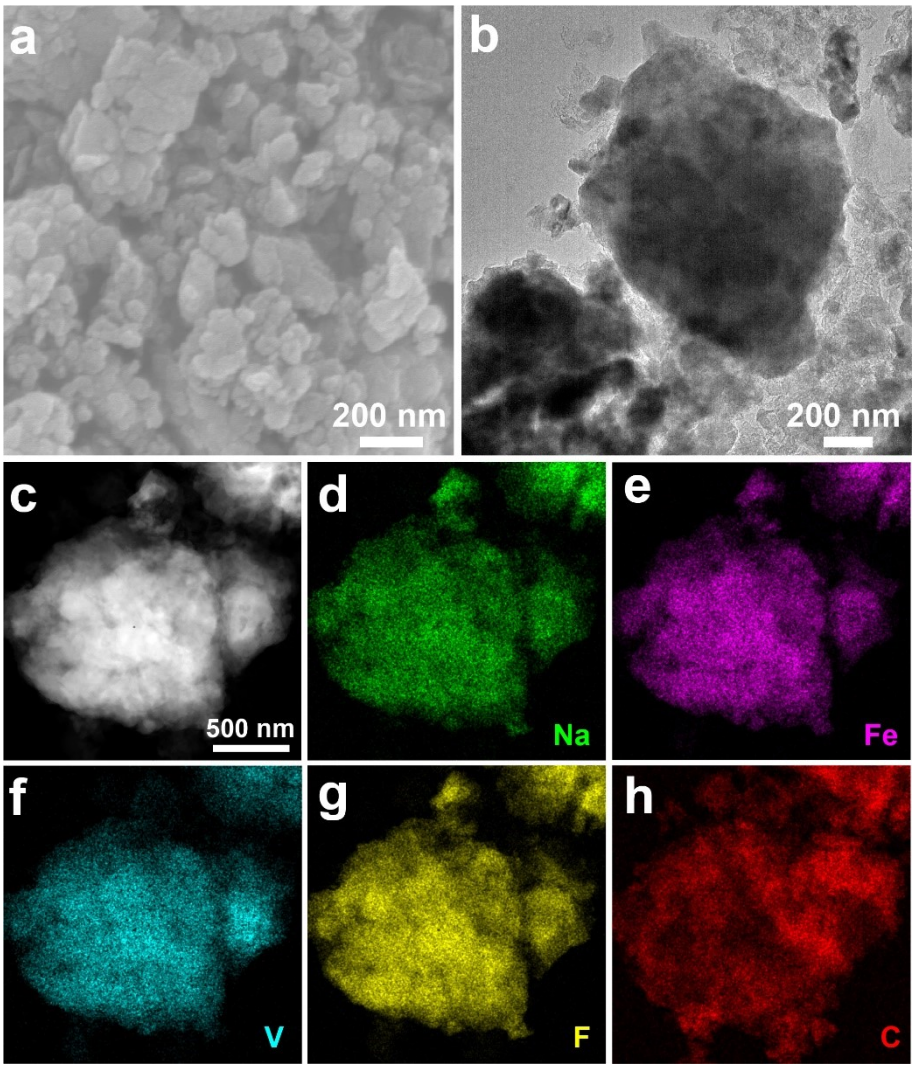

Fig. S11. (a) SEM image, (b) TEM image, (c) scanning transmission electron microscopy image, and (d–h) the corresponding elemental mapping images of the ball-milled Na_2FeVF_7.

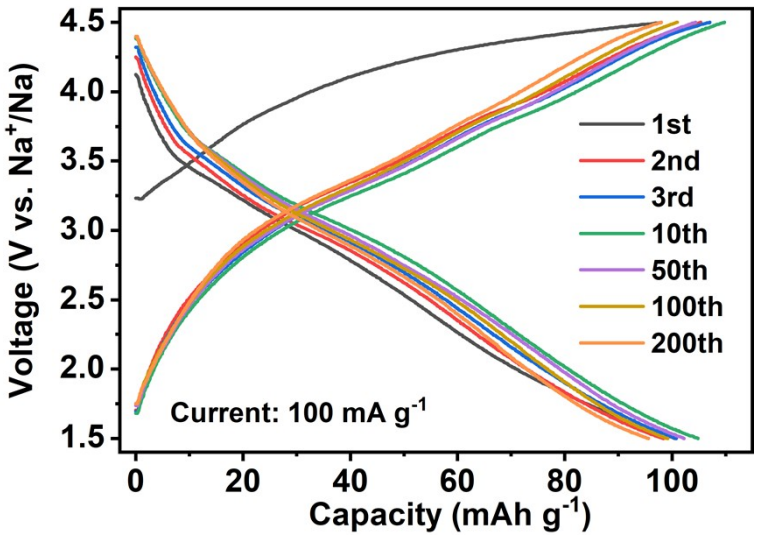

Fig. S12. Selected charge/discharge curves of the Na_2FeVF_7 electrode at 100 mA g^{-1}.

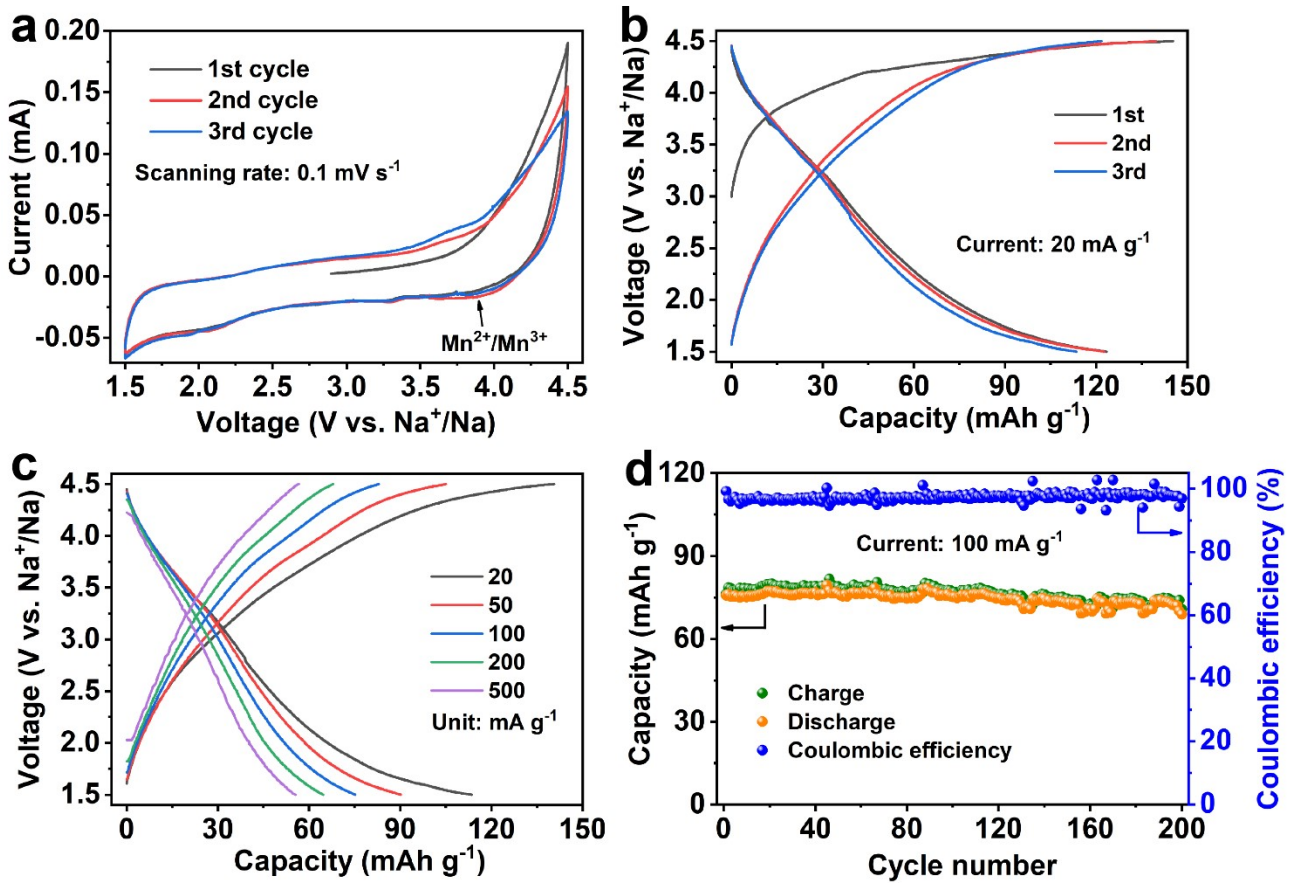

Fig. S13. Electrochemical performance of Na_2MnVF_7: (a) CV curves of the initial three cycles at a scan rate of 0.1 mV s^{-1}; (b) charge/discharge profiles of the initial three cycles at a current density of 50 mA g^{-1}; (c) charge/discharge curves at different current densities; (d) cycling performance at 100 mA g^{-1}.

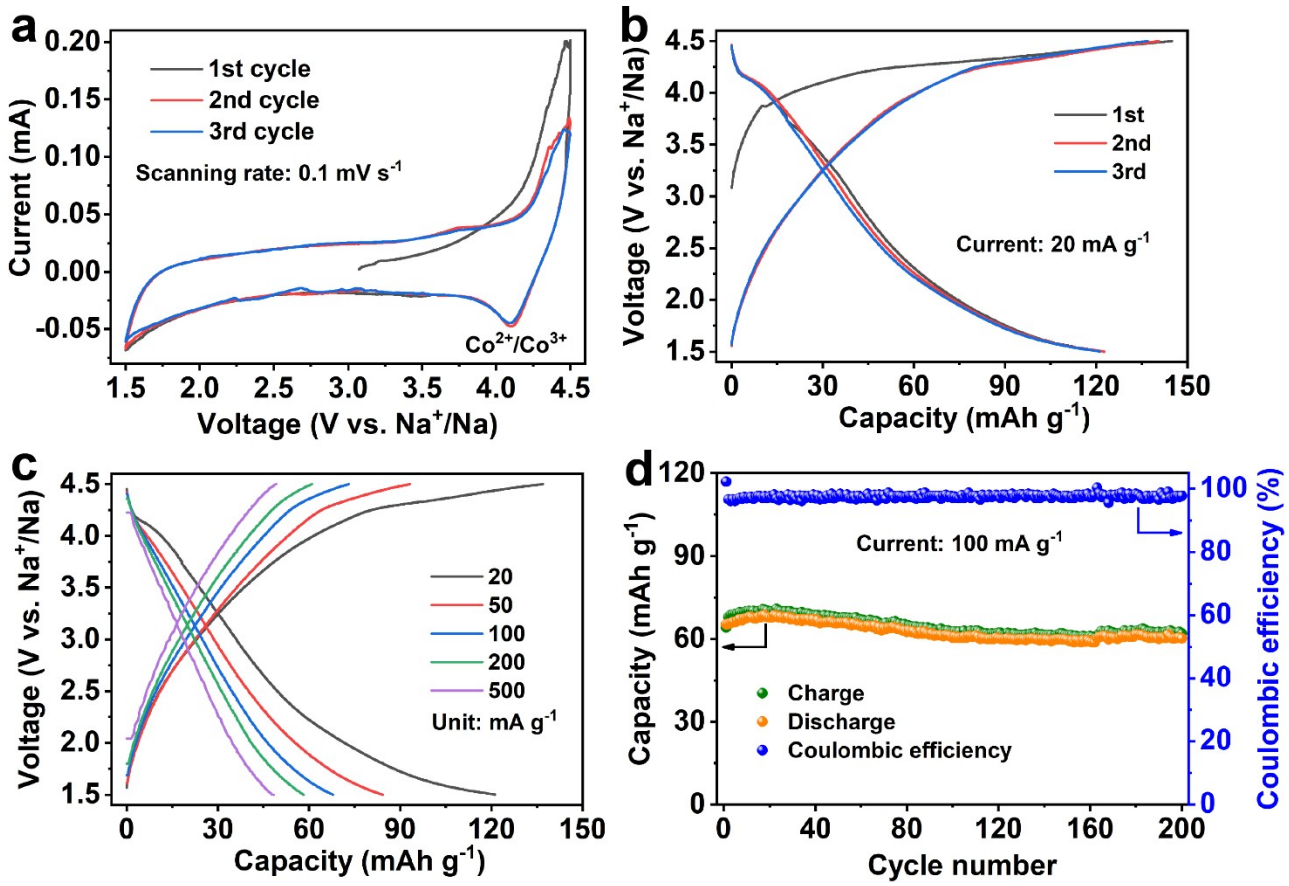

Fig. S14. Electrochemical properties of Na_2CoVF_7: (a) CV curves of the initial three cycles at 0.1 mV s^{-1}; (b) charge/discharge profiles of the initial three cycles at 50 mA g^{-1}; (c) charge/discharge curves at various current rates; (d) cycling performance at 100 mA g^{-1}.

Table S2. Comparison of sodium storage properties of Na_2MVF_7 and other fluoride-based materials.

Samples	Voltage range (V)	Initial charge/discharge capacity (mAh g^{-1})	Cycling stability	References
$FeF_3 \cdot 0.5H_2O$	1.2−4.0	−/135	78% after 50 cycles at 22 mA g^{-1}	2
FeF_3/C	1.2−4.2	−/149	76% after 50 cycles at 20 mA g^{-1}	3
FeF_3/graphene	1.5−4.2	−/206	51% after 50 cycles at 60 mA g^{-1}	4
$K_{0.6}FeF_3$	1.5−4.5	127/140	78% after 10 cycles at 20 mA g^{-1}	5
$KFeF_3$	1.5−4.5	180/110	95% after 35 cycles at 18 mA g^{-1}	6
NH_4FeF_3	2.0−4.5	220/180	85% after 100 cycles at 18 mA g^{-1}	7
Na_3FeF_6	0.65−4.0	−/180	22% after 20 cycles at 17 mA g^{-1}	8
$NaMnF_3$	1.0−4.5	165/130	58% after 15 cycles at 8 mA g^{-1}	9
Orthorhombic $Na_2Fe_2F_7$	2.6−3.8	58/58	86% after 30 cycles at 18 mA g^{-1}	10
Trigonal $Na_2Fe_2F_7$	1.5−4.3	82/184	88% after 1000 cycles at 368 mA g^{-1}	11
Na_2FeVF_7	**1.5−4.5**	**186/147**	**95% after 200 cycles at 100 mA g^{-1}**	**This work**
Na_2MnVF_7	1.5−4.5	146/124	93% after 200 cycles at 100 mA g^{-1}	This work
Na_2CoVF_7	1.5−4.5	145/123	92% after 200 cycles at 100 mA g^{-1}	This work

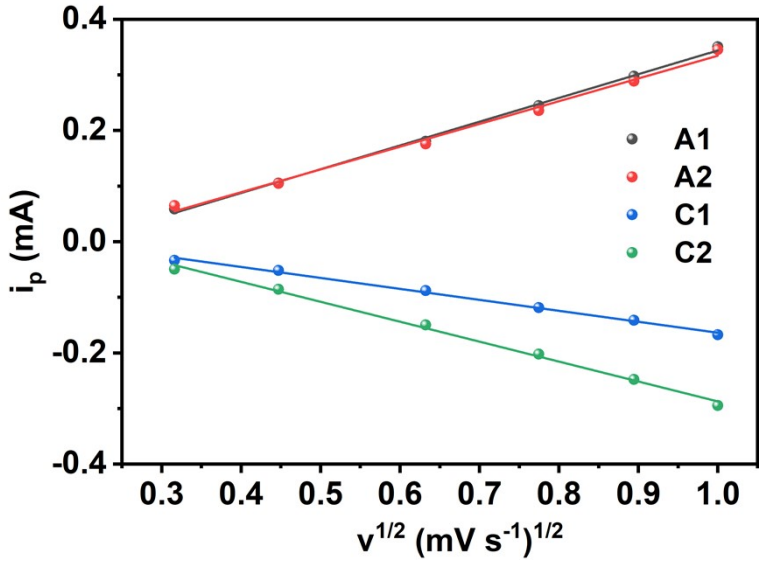

Fig. S15. Linear fitting for the peak current densities (i_p) versus the square root of sweep rates ($v^{1/2}$) achieved from CV curves of Na_2FeVF_7.

Table S3. Na^+ diffusion coefficient of (D_{Na+}) of the Na_2FeVF_7 electrode calculated from CV curves.

Peak	$D_{Na+}/10^{-11}$ **cm^2 s^{-1}**
A1	7.7
A2	7.0
C1	1.6
C2	5.4

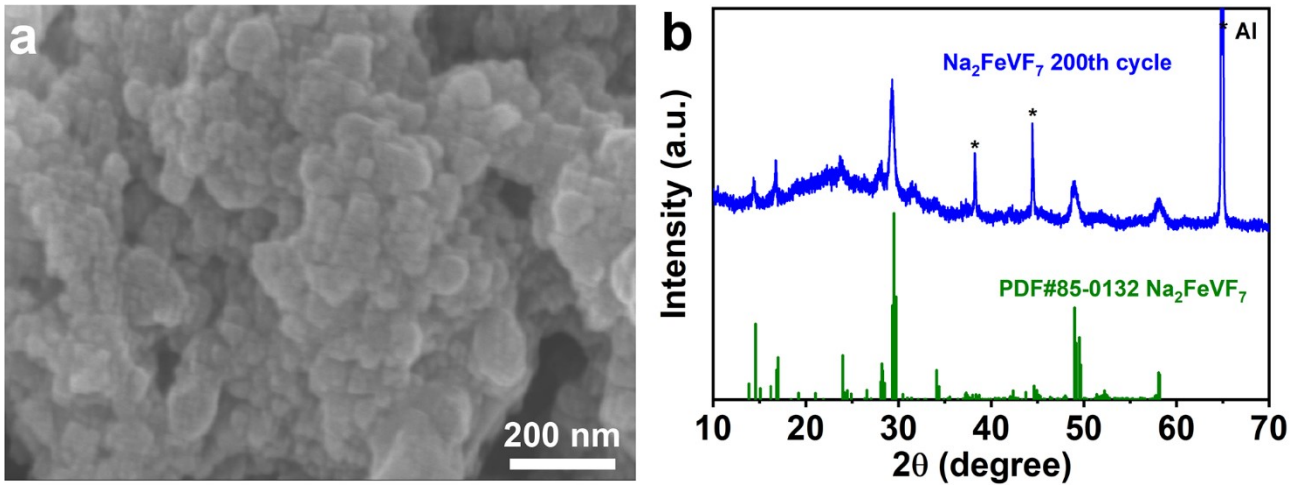

Fig. S16. (a) SEM image and (b) XRD pattern of the ball-milled Na_2FeVF_7 electrode after 200 cycles.

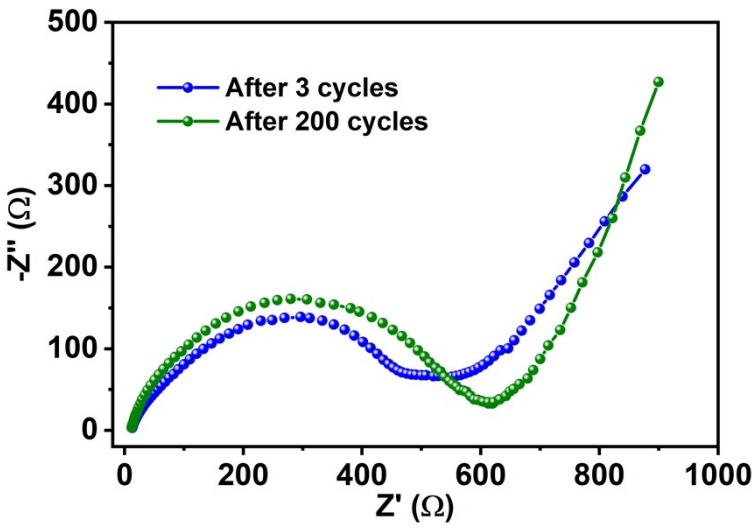

Fig. S17. EIS spectra of the ball-milled Na_2FeVF_7 electrodes after 3 and 200 cycles.

References

1. B. H. Toby, *J. Appl. Cryst.*, 2001, **34**, 210–213.
2. C. Li, C. Yin, L. Gu, R. E. Dinnebier, X. Mu, P. A. Aken and J. Maier, *J. Am. Chem. Soc.*, 2013, **135**, 11425–11428.
3. Z. Sun, W. Fu, M. Z. Liu, P. Lu, E. Zhao, A. Magasinski, M. Liu, S. Luo, J. McDaniel and G. Yushin, *J. Mater. Chem. A*, 2020, **8**, 4091–4098.
4. T. Bao, H. Zhong, H. Zheng, H. Zhan and Y. Zhou, *Mater. Lett.*, 2015, **158**, 21–24.
5. Y. Han, J. Hu, C. Yin, Y. Zhang, J. Xie, D. Yin and C. Li, *J. Mater. Chem. A*, 2016, **4**, 7382–7389.
6. D. Cao, C. Yin, D. Shi, Z. Fu, J. Zhang and C. Li, *Adv. Funct. Mater.*, 2017, **27**, 1701130.
7. A. Martin, E. S. Santiago, E. Kemnitz and N. Pinna, *ACS Appl. Mater. Interfaces*, 2019, **11**, 33132–33139.
8. E. E. Foley, A. Wong, R. C. Vincent, A. Manche, A. Zaveri, E. Gonzalez-Correa, G. Menard and R. J. Clement, *Phys. Chem. Chem. Phys.*, 2021, DOI: 10.1039/d1cp02763h.
9. J. Nava-Avendaño, M. E. A. Dompablo, C. Fronter, J. A. Ayllón and M. R. Palacín, *Solid State Ionics*, 2015, **278**, 106–113.
10. U. K. Dey, N. Barman, S. Ghosh, S. Sarkar, S. C. Peter and P. Senguttuvan, *Chem. Mater.*, 2019, **31**, 295–299.
11. H. Park, Y. Lee, M.-K. Cho, J. Kang, W. Ko, Y. H. Jung, T.-Y. Jeon, J. Hong, H. Kim, S.-T. Myung and J. Kim, *Energy Environ. Sci.*, 2021, **14**, 1469–1479.